

This is an electronic reprint of the original article. This reprint may differ from the original in pagination and typographic detail.

---

## Synthesis of carbon nanotubes on Fe<sub>x</sub>O<sub>y</sub> doped Al<sub>2</sub>O<sub>3</sub>-ZrO<sub>2</sub> nanopowder

Nikkanen, Juha-Pekka; Harju, Mika; Järn, Mikael; Linden, Johan; Rintala, Jyri; Messing, Maria E.; Huttunen-Saarivirta, Elina; Saarinen, Tuomo; Kanerva, Tomi; Honkanen, Mari; Aromaa, Mikko; Levänen, Erkki; Pettersson, Mika; Mäkelä, Jyrki M.; Deppert, Knut; Mäntylä, Tapio

*Published in:*  
Powder Technology

*DOI:*  
[10.1016/j.powtec.2014.06.020](https://doi.org/10.1016/j.powtec.2014.06.020)

Published: 01/01/2014

[Link to publication](#)

*Please cite the original version:*

Nikkanen, J.-P., Harju, M., Järn, M., Linden, J., Rintala, J., Messing, M. E., Huttunen-Saarivirta, E., Saarinen, T., Kanerva, T., Honkanen, M., Aromaa, M., Levänen, E., Pettersson, M., Mäkelä, J. M., Deppert, K., & Mäntylä, T. (2014). Synthesis of carbon nanotubes on Fe<sub>x</sub>O<sub>y</sub> doped Al<sub>2</sub>O<sub>3</sub>-ZrO<sub>2</sub> nanopowder. *Powder Technology*, 266, 106–112. <https://doi.org/10.1016/j.powtec.2014.06.020>

### General rights

Copyright and moral rights for the publications made accessible in the public portal are retained by the authors and/or other copyright owners and it is a condition of accessing publications that users recognise and abide by the legal requirements associated with these rights.

### Take down policy

If you believe that this document breaches copyright please contact us providing details, and we will remove access to the work immediately and investigate your claim.



# Synthesis of carbon nanotubes on $\text{Fe}_x\text{O}_y$ doped $\text{Al}_2\text{O}_3\text{-ZrO}_2$ nanopowder



Juha-Pekka Nikkanen <sup>a,\*</sup>, Mika Harju <sup>a</sup>, Mikael Järn <sup>c</sup>, Johan Linden <sup>d</sup>, Jyri Rintala <sup>e</sup>, Maria E. Messing <sup>f</sup>, Elina Huttunen-Saarivirta <sup>a</sup>, Tuomo Saarinen <sup>a</sup>, Tomi Kanerva <sup>a</sup>, Mari Honkanen <sup>a</sup>, Mikko Aromaa <sup>b</sup>, Erkki Levänen <sup>a</sup>, Mika Pettersson <sup>e</sup>, Jyrki M. Mäkelä <sup>b</sup>, Knut Deppert <sup>f</sup>, Tapio Mäntylä <sup>a</sup>

<sup>a</sup> Department of Materials Science, Tampere University of Technology, P.O. Box 589, FIN-33101 Tampere, Finland

<sup>b</sup> Department of Physics, Aerosol Physics Laboratory, Tampere University of Technology, P.O. Box 692, FIN-33101 Tampere, Finland

<sup>c</sup> Laboratory for Physical Chemistry, Åbo Akademi University, 20500 Åbo, Finland

<sup>d</sup> Physics Department, Åbo Akademi University, FIN-20500 Turku, Finland

<sup>e</sup> Nanoscience Center, Department of Chemistry, P.O. Box 35, FIN-40014, University of Jyväskylä, Finland

<sup>f</sup> Solid State Physics, Lund University, Box 118, 22100 Lund, Sweden

## ARTICLE INFO

### Article history:

Received 11 September 2013

Received in revised form 5 June 2014

Accepted 13 June 2014

Available online 21 June 2014

### Keywords:

Ceramics

Oxides

Nanopowder

Carbon nanotubes

## ABSTRACT

Carbon nanotubes (CNTs) were synthesized on liquid flame sprayed (LFS) powder substrate of iron oxide doped  $\text{Al}_2\text{O}_3\text{-ZrO}_2$ . Iron oxide doped  $\text{Al}_2\text{O}_3\text{-ZrO}_2$  nanopowder was produced by injecting the liquid precursor of aluminium-isopropoxide, zirconium-*n*-propoxide, ferrocene and *p*-xylene into a high temperature (~3000 K) flame. The precursor solution was atomized by high-velocity  $\text{H}_2$  flow and injected into the flame where nanoparticles were formed. The collected sample was used as a substrate material for the synthesis of CNTs. The CNTs were formed on the surfaces of the substrate powder by catalyzed decomposition of  $\text{CH}_4$ . The particle morphology, size, phase composition and the nature of CNTs were determined by TEM, FE-SEM, XRD, XPS, Mössbauer and Raman spectroscopy. The collected powder consists of micron-sized agglomerates with nanosized primary particles. Tetragonal zirconia was detected while alumina was amorphous. In the carbonized sample multiwalled CNTs were obtained.

© 2014 Elsevier B.V. All rights reserved.

## 1. Introduction

Carbon nanotubes (CNTs) have attracted increasing academic and industrial attention in recent years because of their potential for applications in various technologies. CNTs have been of interest due to their unique properties such as high tenacity, flexural rigidity, high electron conductivity, and semiconducting properties [1,2]. These properties combined with excellent chemical stability make them suitable for different applications as functional and reinforcing elements in composites [3–5]. The addition of CNTs to polymer-matrix materials can enhance the electrostatic discharge and the protection against radio frequency interference in aircraft applications [6]. It has also been found that adding a small amount of CNTs improves the antistatic characteristics of the polymer-based materials [7]. Despite the fact that the research on the role of CNTs in composites has mainly focused on polymer-based composites, the CNTs have also been studied as reinforcing agents in metals, such as aluminium [8–10]. The mixing of CNTs into aluminium powder enhances mechanical properties like tensile strength, yield strength and Young's modulus in aluminium strips produced by rolling technique [11].

For ceramic materials, the most important parameters concerning mechanical properties are resistance to crack growth or toughness. Much research for the improvement of toughness has been done on  $\text{ZrO}_2$ -toughened  $\text{Al}_2\text{O}_3$ , which is connected to the phase transition of  $\text{ZrO}_2$  from the tetragonal to the monoclinic phase [12]. The incorporation of CNTs into the ceramics is consequently aimed at enhancing toughness [13]. Considerable improvement in fracture toughness has been observed for example in CNT filled nanosized alumina ( $\text{Al}_2\text{O}_3$ ) and mullite ( $3\text{Al}_2\text{O}_3 \cdot 2\text{SiO}_2$ ) matrix [14,15]. In the case of zirconia ( $\text{ZrO}_2$ ), the addition of CNTs has not been observed to increase the hardness or toughness of sintered monolithic zirconia. However, the electrical resistivity of such material has been significantly decreased as a result of CNT addition [16]. It has also been observed that CNTs in the zirconia matrix hinder the phase transition from cubic  $\text{ZrO}_2$  to monoclinic  $\text{ZrO}_2$  at room temperature [17].

CNTs have been normally generated by releasing carbon atoms from a precursor followed by diffusion of the released atoms, and nucleation and growth of CNTs on a supporting surface [18]. The major methods to fabricate CNTs are arc-discharge technique [19], laser vaporization [20] and chemical vapor deposition (CVD) which is based on the catalytic decomposition of hydrocarbons on catalytic particles (Ni, Co, Fe) [21, 22]. The CVD is the most promising method due to its low cost, high yield and because it is easily controlled. Temperature is one of the most important parameters that need to be controlled in CVD synthesis. The

\* Corresponding author. Tel.: +358 40 849 0193; fax: +358 3 3115 2330.  
E-mail address: [juha-pekka.nikkanen@tut.fi](mailto:juha-pekka.nikkanen@tut.fi) (J.-P. Nikkanen).

required temperature for synthesizing single-walled carbon nanotubes (SWNTs) is normally higher (typically 900–1200 °C) than that required for multi-walled nanotubes (MWNTs): the latter of which is typically 700–900 °C [23]. The CVD process enables the deposition on flat surfaces as well as on powders used to support catalyst particles [21,24]. One benefit in CVD process is that the length of the CNTs can be controlled by adjusting the growth time in the furnace. According to literature, the length of the CNTs increases with an increase in the growing time [25]. Several processes have been proposed to fabricate CNT/ceramic composites such as molecular level mixing process [26] and sol-gel process [27]. In these processes, the commercially produced CNTs have been added into a suspension containing alumina precursor.

In this paper, we describe a novel route to produce composite material consisting of (MWNTs) on the nanosized iron oxide doped  $\text{Al}_2\text{O}_3\text{-ZrO}_2$  powder produced by the liquid flame spray (LFS) method. LFS opens up a possibility to produce multicomponent oxide nanomaterials together with an additional catalyst needed for the growth of CNTs. The benefit of this approach is that the multicomponent substrate for CNT generation is produced by a single process and obtained CNTs are well dispersed into the porous substrate. Moreover, according to the literature, it is possible to adjust the size of the produced nanoparticles by changing the parameters, such as concentration of the precursor, in the LFS process [28]. However, in this work, the main interest was to examine, whether the prepared composite powder could be used as a catalyzing substrate for the CNT growth.

The produced material is carefully analyzed in order to determine the resulting particle size, morphology, phases and chemical composition at the different stages of processing, i.e., before and after the CNT growth, and the results from such analysis work are presented in this paper.

## 2. Experimental

### 2.1. LFS process and setup for the synthesis of carbon nanotubes

The aluminium isopropoxide ( $\text{C}_9\text{H}_{21}\text{AlO}_3$ ), zirconium (IV) n-propoxide ( $\text{Zr}[\text{O}(\text{CH}_2)_2\text{CH}_3]_4$ ) and ferrocene ( $(\text{C}_5\text{H}_5)_2\text{Fe}$ ) were dissolved in p-xylene to ensure full solubility of all compounds. This liquid ready-mixed feedstock was atomized into micron sized droplets by high velocity  $\text{H}_2$  flow and fed into a turbulent, high-temperature ( $T \sim 3000$  K)  $\text{H}_2\text{-O}_2$ -flame where nanoparticles were formed. The concentrations of aluminium isopropoxide, zirconium (IV) n-propoxide and ferrocene in p-xylene solution were 1.2 M, 0.50 M and 0.18 M respectively. Liquid feeding rate was 30 ml/min and the flow of gases was 150 l/min  $\text{H}_2$  and 25 l/min  $\text{O}_2$ . LFS process was realized in air atmosphere. The particles were collected by a cylindrical electrostatic precipitator using a 6.0 kV voltage on the central rod and 0.3 mA current from rod to grounded cylinder. The LFS process is schematically illustrated in Fig. 1.

The produced composite nanopowder was used as a substrate material for the CNTs. CNTs were grown on this substrate material by decomposition of methane ( $\text{CH}_4$ ) at 800 °C. The process temperature was selected in order to produce MWNTs instead of SWNTs which are formed at higher temperature according the literature [23]. A certain amount of the substrate material was placed in a u-shaped sample cell made of silica glass. After that the sample cell was evacuated (pressure < 1.33 mPa) with simultaneous heating to 800 °C. The evacuation was performed to

avoid oxidation in the next step. After reaching the desired vacuum level the methane gas was fed into the sample cell for 1 h. The gas pressure was 107 kPa and the temperature was 800 °C. The growth cycle was repeated four times to provide sufficient deposition of CNTs.

### 2.2. Characterization

The crystal structure of the powder substrate was determined before and after the carbonization by an X-ray diffractometer (Kristalloflex D-500, Siemens) using monochromatized  $\text{CuK}\alpha$  radiation. The morphology of the particles and CNTs was determined by a transmission electron microscope (TEM) (JEOL, JEM 2010), a field emission scanning electron microscope (FE-SEM) (ZEISS, ULTRAPLUS) and a high resolution transmission electron microscope (HR-TEM) (JEOL, JEM 3000F) equipped with an X-ray energy dispersive spectrometer (EDS). The XPS measurements were performed with a Physical Electronics Quantum 2000 instrument equipped with a monochromatic Al  $\text{K}\alpha$  X-ray source. An operating power of 25 W was used with a spot diameter of 100  $\mu\text{m}$ . An electron flood gun and a low energy ion gun were used for charge compensation. The detector position was at an angle of 45° in relation to the sample surface. The low and high resolutions of pass energy in spectral acquisition were 117.4 and 23.5 eV, respectively. Surface concentrations were determined with the MultiPak 6.1 software using peak areas to give surface concentrations in atomic percent. The binding energies (BEs) were referenced to that of the adventitious carbon 1s peak at 285.0 eV.

The Mössbauer absorbers were made by evenly distributing ~30 mg of the sample material together with an epoxy resin across an area of ~3.0  $\text{cm}^2$  on a thin Al foil. The measurements were done in transmission geometry using a Cyclotron Co. source  $^{57}\text{Co:Rh}$  (25 mCi, Jan 2004) at a fixed temperature of 77 or 300 K. The maximum Doppler velocity was 4.0 mm/s for the paramagnetic sample and 6.0 for the sample exhibiting magnetic splitting. Samples exhibiting magnetic splitting were fitted with the full Hamiltonian of combined electric and magnetic interactions using the following parameters: the internal magnetic field components ( $I$ ), the resonance line widths ( $\Gamma$ ), constrained to be equal for all spectral components, the quadrupole coupling constant ( $eQV_{zz}$ ), the asymmetry parameter ( $\eta$ ) and the angle  $\beta$  between the directions of B and  $V_{zz}$ . For the paramagnetic case the fit parameters were  $I$ ,  $\Gamma$ ,  $\delta$  and  $eQV_{zz}$ .

The Raman measurements were performed with a home-built Raman spectrometer in a back-scattering geometry using two different excitation wavelengths: 532 nm (Alphas Monolas-532-100-SM) and 632.8 nm (Melles Griot 25-LHP-991-230). The Rayleigh scattering was attenuated with an edge filter (Semrock) allowing recording of Raman spectrum down to 70  $\text{cm}^{-1}$ . The scattered light was dispersed in a 0.5 m imaging spectrograph (Acton SpectraPro 2555i) using a 600 g/mm grating. The signal was detected with an EMCCD camera (Andor Newton EM DU971N-BV) using a 100  $\mu\text{m}$  slit width. The signal was accumulated from 300 measurements 0.5 s each to obtain a better signal to noise ratio.

Thermogravimetric analysis (TG) was performed using a Netzsch STA 409 Thermal Analyzer. The measurements were carried out in the temperature range of 50–850 °C at a heating rate of 5 °C/min in a flowing air atmosphere (60  $\text{cm}^3/\text{min}$ ). The sample masses were in the range of 8–10 mg.

## 3. Results and discussion

### 3.1. XRD analysis of crystal structures

The XRD diffraction pattern of the LFS synthesized powder measured before CNT growth (Fig. 2a) shows the formation of tetragonal  $\text{ZrO}_2$ . Since no other crystalline phases in addition to tetragonal zirconia were detected, alumina and iron oxide are probably in non-crystalline form or the amount is below the detection limit of XRD. Curve 2 (b) shows

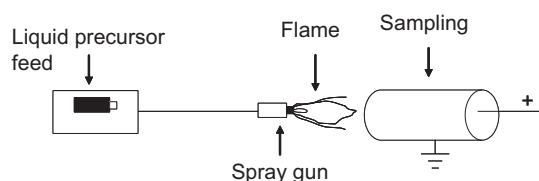


Fig. 1. Schematic description of the LFS-process [29,30].

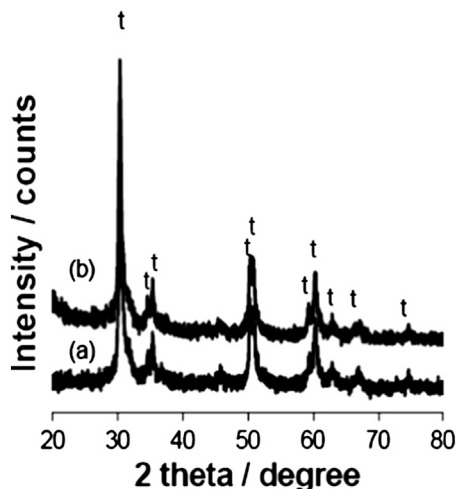


Fig. 2. XRD diffraction pattern of the LFS synthesized powder (a) and the powder with CNTs (b); t: tetragonal zirconia.

the sample after decomposition of methane. The curves 2 (a) and (b) are almost identical. Hence, no crystallization of new phases or crystal growth of tetragonal zirconia was detected after CNT growth. The crystallite size of *t*-ZrO<sub>2</sub> was estimated from XRD pattern by Scherrer's formula  $t = (0.9\lambda / B \cos \theta)$  [31], where *t* is the diameter in nm,  $\lambda$  is the wavelength of X-ray radiation (0.15418 nm), *B* is the full width at half maximum in radians and  $\theta$  is the Bragg angle. The full width at half maximum for both samples was  $\sim 5.6 \times 10^{-3}$  rad and the peak was present at approximately 30.2° in 2 $\theta$ . The calculation of crystallite size gave the size of  $\sim 25$  nm for *t*-ZrO<sub>2</sub> in both samples.

The stable polymorph of zirconia at low temperatures and at atmospheric pressure is the monoclinic crystal structure. The martensitic transition from monoclinic to tetragonal phase upon heating occurs approximately at 1150 °C, whereas reverse transition upon cooling occurs at about 900 °C [32,33]. The critical crystal size for phase transition from tetragonal to monoclinic is 8–18 nm. Below above-mentioned range tetragonal phase is thermodynamically stable [30]. Tetragonal structure could, in certain circumstances, occur although the crystal size is bigger than 18 nm. Rapid cooling of nanoparticles during the synthesis could quench zirconia into tetragonal form even if the crystal size is > 18 nm [32]. It is also reported that the critical size of tetragonal zirconia has different values when the zirconia is dispersed in various matrices [34]. According to the literature, the grain growth of zirconia is inhibited as the zirconia grains are embedded in alumina matrix [35]. Thereby, the results from XRD measurements suggest the presence of zirconia featuring the average grain size of 25 nm, with the tetragonal structure being possibly stabilized by the other phases present.

### 3.2. XPS analysis of oxidation states of Al, Zr, and Fe

The aim of the XPS measurements was to verify the oxide phases present and, particularly, to clarify the oxidation states of the iron catalyst on the substrate material. The XPS survey spectra of the LFS synthesized sample and further carbonized sample are shown in Fig. 3. In both spectra, the Al 2p peak position around 74 eV and the Zr 3d<sub>5/2</sub> peak position around 182 eV indicate that both Al and Zr are present and oxidized to Al<sub>2</sub>O<sub>3</sub> and ZrO<sub>2</sub>, respectively. Similarly, in both cases, the peak position of Fe 2p<sub>3/2</sub> at around 711.5 eV is compatible with trivalent Fe, possibly Fe<sub>2</sub>O<sub>3</sub>. Adventitious carbon was detected from the wide-scan spectra at around 285 eV and 197 eV. This carbon is residue from organics used in LFS. Also a minor peak indicating the presence of traces of chlorine was detected at around 197 eV. The origin of this minor peak is most probably from the test environment. The XPS spectrum of the iron oxide doped sample is nearly similar to the spectrum of the carbonized sample. The only obvious difference is the

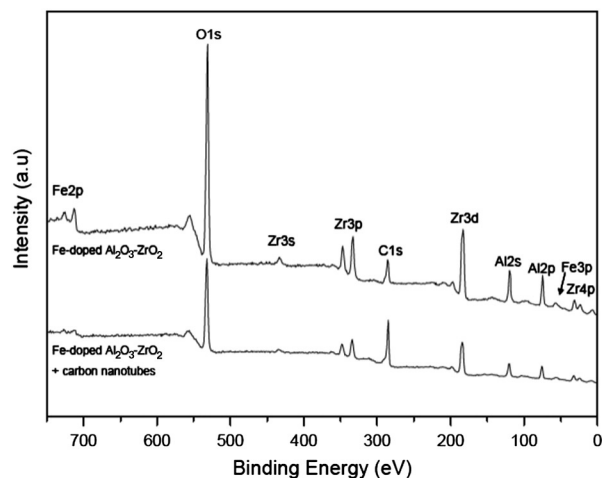


Fig. 3. XPS survey spectra of iron-oxide doped Al<sub>2</sub>O<sub>3</sub>-ZrO<sub>2</sub> and carbonized sample.

higher intensity of the carbon peak at around 285 eV of the carbonized sample. Reduction of the Fe<sub>2</sub>O<sub>3</sub> is not observed from the XPS spectra of the carbonized sample. This is probably because the sample was in contact with ambient air before the XPS measurements and this made the reoxidation of Fe possible. Also, Fe<sup>3+</sup>, Fe<sup>2+</sup> and Fe<sup>0</sup> peaks overlap which complicates the analysis. Characteristic peak positions for the Fe 2p signal are 711.2 eV and 724.3 eV for Fe<sup>3+</sup>, 709.8 and 722.8 eV for Fe<sup>2+</sup> and 706.8 eV and 719.8 eV for Fe<sup>0</sup> [36]. Therefore, the presence of Fe<sub>3</sub>O<sub>4</sub> cannot be completely ruled out according to XPS results. To summarize, XPS spectra reveal the presence of Al<sub>2</sub>O<sub>3</sub>, ZrO<sub>2</sub> and trivalent iron, possibly Fe<sub>2</sub>O<sub>3</sub>, in both LFS and carbonized specimens. However, also the presence of Fe<sup>2+</sup> and metallic Fe is possible due to peak overlapping, and the presence of oxidized Fe in carbonized specimen may be due to exposure to ambient air.

### 3.3. Mössbauer analysis of oxidation states of Fe

Mössbauer spectroscopy was used in addition to XPS measurements to get more information about the oxidation states of iron in LFS synthesized powder and after CNT growth. Mössbauer spectroscopy offers several advantages for the research of iron compounds. One of the main merits of Mössbauer spectroscopy is that it readily facilitates identification of divalent and trivalent Fe species. In Fig. 4 the 300 K spectrum of the LFS-synthesized iron oxide doped Al<sub>2</sub>O<sub>3</sub>-ZrO<sub>2</sub> sample is shown. The spectrum consists of a slightly asymmetric doublet and

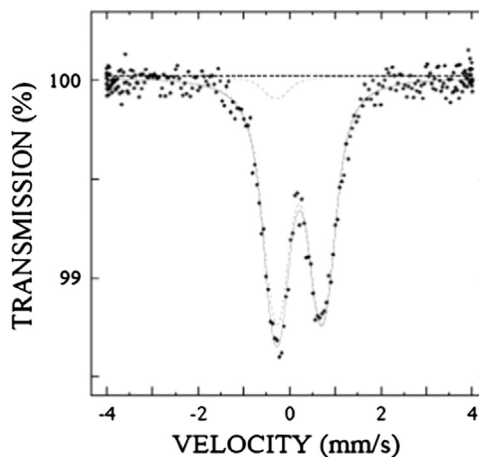


Fig. 4. Mössbauer spectrum of the iron oxide doped Al<sub>2</sub>O<sub>3</sub>-ZrO<sub>2</sub> sample. The two paramagnetic components used in the fitting are shown.

is conveniently fitted using a singlet (having almost zero quadrupole interaction) and a doublet. The isomer shifts for the singlet (covering 8.3% of the spectral area) and the doublet (91.7% of spectral area) are  $-0.169$  mm/s and  $0.327$  mm/s, respectively. Both are typical for trivalent Fe. The absence of an internal field does not rule out  $\text{Fe}_2\text{O}_3$ , as nanoparticles are known to exhibit purely paramagnetic spectra [37], in particular as the XRD patterns suggest that the Fe-rich phase is non-crystalline. The experimental line widths are very much broadened, which was modeled by allowing a Gaussian distribution of the quadrupole coupling constant. This is also indicative of a strong non-crystalline character of the Fe phase. Given that the Fe phase consists of nanoparticles of  $\text{Fe}_2\text{O}_3$  the average particle size should be less than  $\sim 13$  nm [37]. This is probably due to Fe atoms on the surface layer of the  $\text{Fe}_2\text{O}_3$  nanoparticles: Assuming an  $\sim 0.3$  nm thick surface layer then  $\sim 10\%$  of the Fe atoms will be located on the surface of a spherical particle, in rough agreement with the intensity of the singlet component.

The carbonized sample exhibits a distinct magnetic splitting both at 300 K and 77 K, Fig. 5. Three components were needed to fit the spectra. The hyperfine parameters are listed in Table 1. The three components used in the fittings are displayed above the data. Judging by the isomer shift Component 1 is due to trivalent Fe. However, both the quadrupole coupling constant and the internal field of 25 T are too small for  $\text{Fe}_2\text{O}_3$ . The paramagnetic component (Component 3) has an isomer shift which is compatible with trivalent Fe. It has a rather small quadrupole coupling constant and could therefore originate from a similar surrounding as Component 1. A more probable explanation to the observations is that the nanoparticles consist of metallic Fe, as these would due to the size of  $\sim 12$  nm in the superparamagnetic state. The rather small quadrupole coupling constant and the isomer shift to zero velocity are compatible with this conclusion. Also the presence of  $\text{Fe}^{2+}$  indicates that the carbonization conditions were reductive. Component

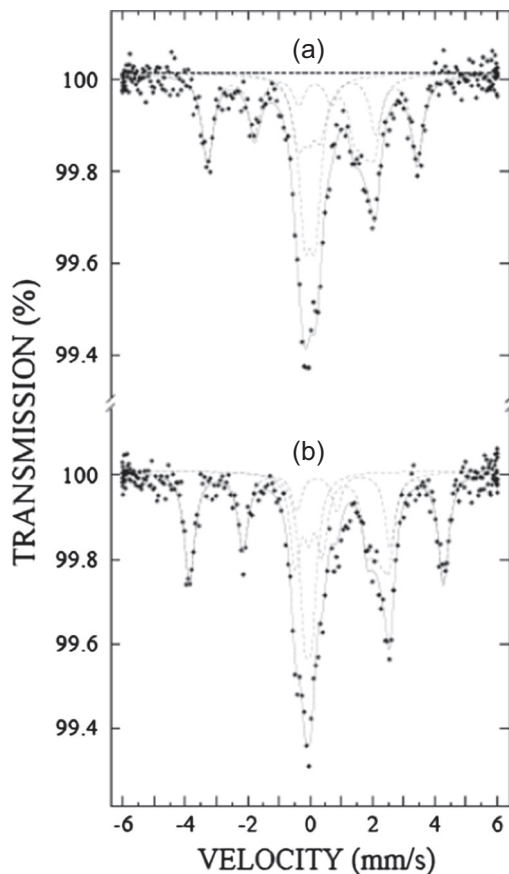


Fig. 5. Mössbauer spectra of the carbonized  $\text{Al}_2\text{O}_3\text{-ZrO}_2$  sample recorded at (a) 300 K and (b) 77 K.

Table 1  
Hyperfine parameters of the carbonized sample.

	Component	B(T)	$\delta$ (mm/s)	$eQV_{zz}$ (mm/s)	$\eta$	$\beta$
300 K	1 (37.4%)	20.8	0.233	-0.18	-	-
	2 (33.3%)	3.4	0.971	3.31	0.5	71
	3 (29.2%)	-	0.113	0.68	-	-
77 K	1 (40.3%)	25.2	0.323	0.00	-	-
	2 (37.2%)	3.8	1.188	4.29	0.28	73
	3 (22.5%)	-	0.056	0.47	-	-

2 is due to high-spin divalent Fe. It has an abnormally large quadrupole coupling constant and an asymmetric shape, which was here modeled by including a small magnetic field, which was not parallel to  $V_{zz}$  (non-zero  $\beta$  angle). Somewhat similar hyperfine parameters have been observed earlier e.g. in divalent Fe species exhibiting orbital ordering in  $\text{EuBaFe}_2\text{O}_5 + w$ . [38]. However, the present data does not allow us to draw detailed conclusions on the presence of divalent Fe species. According to the Mössbauer data the average valence of Fe is between  $+2.6$  and  $+2.7$ . However, the Mössbauer Component 3 clearly refers to the existence of metallic Fe nanoparticles. The decreasing of the oxidation state of Fe from  $+3$  or even more oxidized Fe is most probably due to a reduction caused by hydrogen and carbon released during the decomposition of methane. The average valence of Fe (from  $+2.6$  to  $+2.7$ ) is due to the reoxidation of unprotected iron species in the ambient air before the Mössbauer measurements, and also the presence of metallic Fe is confirmed.

The results from Mössbauer spectroscopy, therefore, disclose that in LFS sprayed state, iron in composite powder is essentially in the trivalent oxidation state. After CNT growth, the average valence is lower, from 2.6 to 2.7, and the presence of metallic Fe is also confirmed, i.e., reduced with respect to the original compound. It is also anticipated that some of the metallic Fe is reoxidized in ambient air, making the true carbonized valence lower than the measured value.

### 3.4. TEM, FE-SEM and HR-TEM micrograph analysis

Typical TEM, FE-SEM and HR-TEM micrographs of the collected samples are shown in Fig. 6. The micrographs give the general view of the iron oxide doped  $\text{Al}_2\text{O}_3\text{-ZrO}_2$  before (Fig. 6a) and after (Fig. 6b and c) the decomposition of methane. The primary particle size as estimated from TEM and HR-TEM micrographs (Fig. 6a and c) is approximately from 12 to 50 nm, whereas the outer diameter of CNTs is about 14 nm. FE-SEM micrograph (Fig. 6b) shows that the CNTs are well dispersed within the ceramic powder and the HR-TEM micrograph (Fig. 6c) reveals the multiwalled nature of CNTs with the inner diameter of approximately 1.4 nm. Fig. 6c is considered to be representative in terms of structure and size of studied CNTs. It is emphasized that although the CNTs that were examined were chosen arbitrarily, SWNTs were not detected at all. However, it does not necessarily mean that there are no SWNTs in the sample, but evidently their fraction is very small as compared to the fraction of MWNTs.

It is well known that the outer diameter of CNTs is largely related to the size of the catalytic particles. According to HR-TEM examination and EDS analyses, the catalyst particles of essentially metallic iron are enclosed inside CNTs (Fig. 6c). Indeed, EDS analysis (EDS 1 in Fig. 6c) revealed only the presence of iron. This means, in practice, that the growth of CNTs follows the tip growth mechanism in which the loosely bonded catalyst particles come off from the support material during the growth of CNTs [23].

The relation between the size of catalyst particles and the outer diameter of CNTs can be clearly seen when comparing the diameter of the catalyst particles (Fe) enclosed inside the CNTs (12 nm) to the outer diameter of CNTs (14 nm). Furthermore, the size of catalyst particles is well consistent with the Mössbauer measurement (Fig. 4) in which

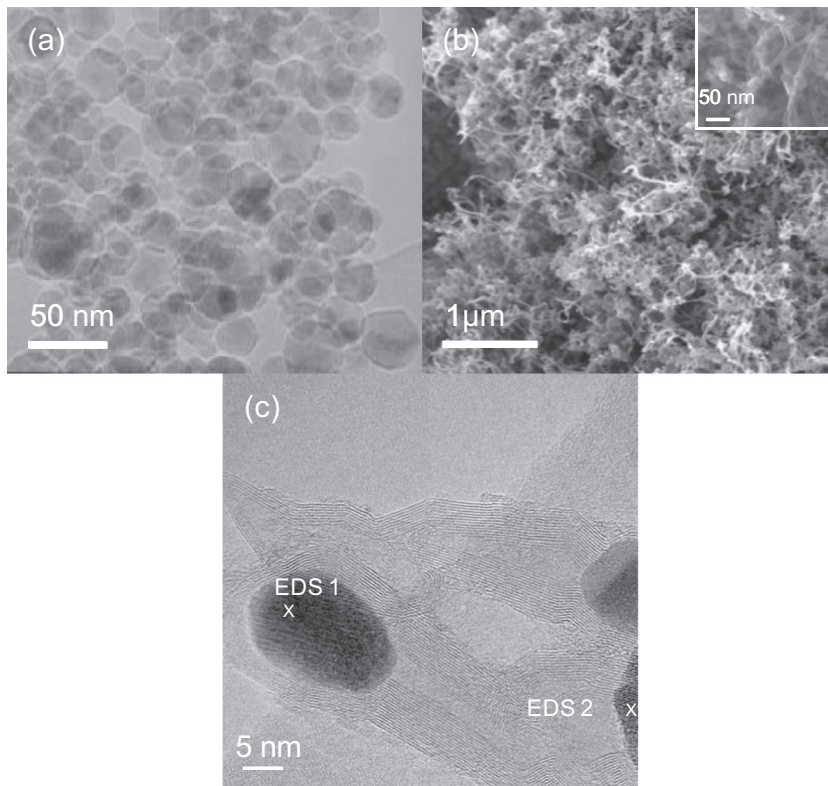


**Fig. 6.** TEM micrograph of iron oxide doped  $\text{Al}_2\text{O}_3\text{-ZrO}_2$  sample (a), FE-SEM micrograph (b) and HRTEM micrograph (c) of the sample with CNTs. EDS 1: Element Fe K (wt.% 100). EDS 2: Element O K (wt.% 37.86), Al K (wt.% 26.16), Zr K (wt.% 30.46), and Fe K (wt.% 5.52).

the average particle size was concluded to be less than 13 nm due to the occurrence of (super) paramagnetic doublet.

According to the Mössbauer measurements, the average valence of Fe after the carbonizing process was between +2.6 and +2.7. However, HR-TEM studies and EDS analysis showed that metallic iron particles are enclosed inside the CNTs. This supports the interpretation of Mössbauer Component 3.

Most recently, it has been extensively confirmed that graphite shells effectively protect the sensitive metal core against oxidation [39]. It is also well known that the CNTs have been used as gas storage materials and it is possible to store gases inside CNTs for long periods either by the opening of CNTs or by hot isostatic pressing (HIP) and following exposure to the gas [23]. On this basis, it does not seem to be possible that the fully encapsulated catalyst particles could oxidize in contact with ambient air after the carbonizing process. Hence, there is a good reason to expect that the valence of Fe decreased from +3 to 0 during the carbonizing process and the metallic iron which finally got trapped inside the CNTs worked as a catalyst for the CNT growth. However, the catalyst particles which were finally only partly encapsulated inside the CNTs may have oxidized after carbonizing process due to contact with ambient air. Thereby, it may be concluded from microstructural examinations that the produced CNTs were MWCNTs and they grew from Fe catalyst particles with a clear dimensional relationship between the two being detected.

### 3.5. Raman analysis of carbon nanotubes

The Raman spectroscopy was used as a tool to characterize the properties and structure of CNTs. The Raman spectrum of the sample measured with 633 and 532 nm excitation is presented in Fig. 7. The appearance of the spectrum is characteristic for a CNT material as evidenced by the G-band at  $1590\text{ cm}^{-1}$ , D-band at  $1326\text{ cm}^{-1}$  and the RBM (radial breathing mode) at  $192\text{ cm}^{-1}$  with a shoulder at  $218\text{ cm}^{-1}$  [40]. The RBM mode was observed with 633 nm excitation.

RBM can originate either from SWNTs or from inner tubes of small-diameter MWNTs. In particular, the observation of the RBM mode which does not appear in graphite or other carbonaceous materials evidences the presence of CNTs in the material. The shape of the G and D bands is characteristic for CNTs [41]. The relatively high intensity of the D band indicates the presence of carbonaceous impurities other than CNTs or defects in the CNT structure. The observation of the RBM mode at  $192\text{ cm}^{-1}$ , which does not appear in graphite, indicates the presence of CNTs with a small diameter. The diameter was calculated

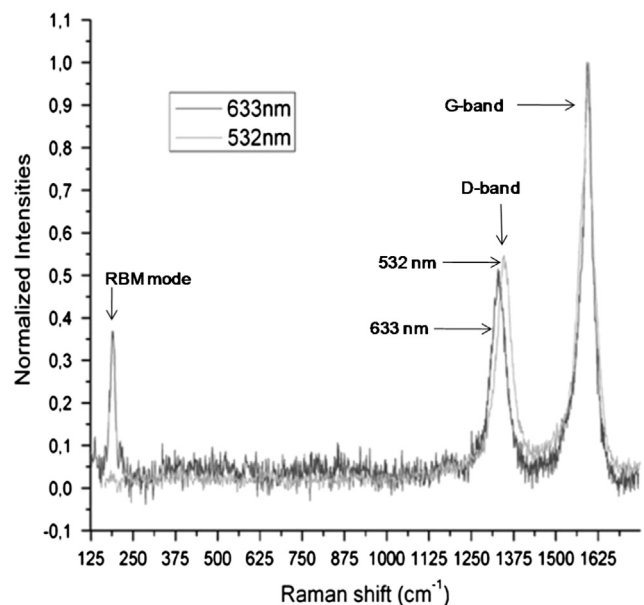


**Fig. 7.** The Raman spectrum of the sample with CNTs measured with 532 and 633 nm excitation.

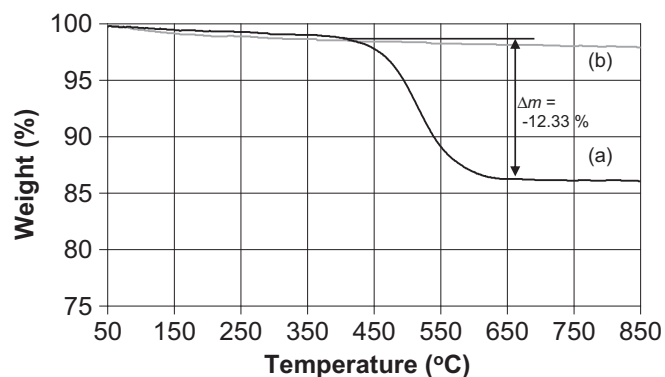


**Fig. 8.** Thermogravimetric analysis of the powder with CNTs (a) and the LFS synthesized powder (b).

by using the relation between the diameter  $d$  (in nm) and the frequency  $\omega_{\text{RBM}}$  (in  $\text{cm}^{-1}$ ) of the RBM mode [42]:

$$\omega_{\text{RBM}} = \frac{218}{d} + 16. \quad (1)$$

The calculation gives the diameter of 1.24 nm. This corresponds to the inner diameter of CNTs and is well consistent with the diameter measured from HR-TEM micrographs (Fig. 6c). The interlayer coupling of the RBM modes in CNTs causes deviation from the relation (1) which is determined for SWNTs and this effect is of current interest [43]. The RBM mode was observed with 633 nm excitation but not with 532 nm excitation while the other features were very similar with the two-excitation wavelengths. This is most probably due to the electronic resonance effect that enhances the signal from those tubes that are in electronic resonance with the excitation laser. All in all, the Raman measurements confirmed the carbonaceous nature of the synthesized tubes and gave support to TEM observations about the inner diameter of the CNTs.

### 3.6. TG analysis

Fig. 8 shows the TG graphs for the powder with CNTs (a) and for the LFS synthesized powder (b). The weight loss of 12.33% was recorded for the powder with CNTs in the temperature range of 437–660 °C. In this temperature range, no significant weight losses occurred in LFS synthesized powder, indicating that the decrease in weight of the carbonized sample was obviously due to the combustion of the CNTs formed during carbon nanotube synthesis [44]. According to XPS and Raman results, there were carbonaceous impurities in both of the studied powders. However, as weight losses at 437–660 °C were only found in the powder with CNTs, it is evident that such impurities play a minor role in the overall weight changes of the powders. The results indicate that the specimens contained 12.33 wt.% of CNTs after carbonization.

## 4. Conclusions

CNTs were generated successfully on the liquid flame sprayed (LFS) substrate of the iron oxide doped  $\text{Al}_2\text{O}_3\text{-ZrO}_2$  by catalyzed decomposition of methane. The crystal structure, particle and crystal size as well as the nature of CNTs were determined by a wide range of methods.

The XRD analyses showed that the structure of alumina is not crystalline, whereas zirconia exists in tetragonal phase. The oxidation state of Fe was +3 before and between +2.6 and +2.7 after the carbonizing process, according to Mössbauer measurements. However, the Mössbauer analysis also refers to the existence of metallic Fe nanoparticles on the carbonized sample. The observed decrease in the oxidation state of Fe is due to a reduction by hydrogen and carbon

released during the decomposition of methane. The average valence of Fe (from +2.6 to +2.7) is probably due to the reoxidation of unprotected iron species in the ambient air before the Mössbauer measurements. According to HR-TEM and EDS analysis, the catalyst particles which are fully enclosed inside the CNTs are metallic iron. This means that the metallic iron acted as a catalyst for CNT growth in this study and that the oxidation of iron occurred only for poorly encapsulated iron particles. HR-TEM of carbonized  $\text{Al}_2\text{O}_3\text{-ZrO}_2$  proved the presence of MWNTs in the sample. The dimensions of the CNTs that were obtained by various methods showed relatively good consistency. The outer diameter of CNTs was found in TEM studies to be approximately 14 nm, while the diameter of the catalyst particles was found to be around 12 nm. Furthermore, the size of catalyst particles is well consistent with the Mössbauer measurements in which the average particle size was concluded to be less than 13 nm. Also, the inner tube diameter in TEM studies was 1.4 nm, while according to Raman analysis it was 1.2 nm. Hence, the results obtained from different methods show relatively good agreement. According to TG analysis, the weight loss of the carbonized sample was 12.33% which shows that a reasonable yield of CNTs (with minor amount of carbonaceous impurities) was obtained.

The liquid flame spray process used in this study can be utilized in a simple one step processing of multicomponent substrate for CNT production. This simple and highly versatile synthesis technique is a promising tool for engineering composite nanoparticles with demanded composition and particle size. The adjustability of particle size of the final product is significant to produce the catalyst particles with tailored size, and due to these CNTs with desired diameter. However, more effort should be put in future studies to study the yield of CNTs by adjusting the process parameters from initial LFS process to final growth of CNTs.

## Acknowledgments

We are grateful to Mr. Mikko Kylmälahti for the assistance in producing our specimens. This work is partially supported by EU research project IP Nanoker (FP-515784-2) and The Finnish National Graduate School on New Materials and Processes.

## References

- [1] R.H. Baughman, A.A. Zakhidov, W.A. de Heer, Carbon nanotubes—the route toward applications, *Science* 297 (2002) 787–792.
- [2] K.T. Lau, D. Hui, The revolutionary creation of new advanced materials—carbon nanotube composites, *Compos. Part B* 33 (2002) 263–277.
- [3] P. Scharff, New carbon materials for research technology, *Carbon* 36 (1998) 481–486.
- [4] D. Tashima, K. Kurosawatsu, M. Uota, T. Karashima, M. Otsubo, C. Honda, Y.M. Sung, Space charge distributions of an electric double layer capacitor with carbon nanotubes electrode, *Thin Solid Films* 515 (2007) 4234–4239.
- [5] N. Yu, Z.H. Zhang, S.Y. He, Fracture toughness and fatigue life of MWCNT/epoxy composites, *Mater. Sci. Eng. A* 494 (2008) 380–384.
- [6] K.T. Lau, S.Q. Shi, Failure mechanisms of carbon nanotube/epoxy composites pretreated in different temperature environments, *Carbon* 40 (2002) 2961–2973.
- [7] J. Sandler, M.S.P. Shaffer, T. Prasse, W. Bauhofer, K. Schulte, A.H. Windle, Development of a dispersion process for carbon nanotubes in an epoxy matrix and the resulting electrical properties, *Polymer* 40 (1999) 5967–5971.
- [8] H.J. Choi, G.B. Kwon, G.Y. Lee, D.H. Bae, Reinforcement with carbon nanotubes in aluminium matrix composites, *Scr. Mater.* 59 (2008) 360–363.
- [9] C.F. Deng, D.Z. Wang, X.X. Zhang, A.B. Li, Processing and properties of carbon nanotubes reinforced aluminium composites, *Mater. Sci. Eng. A* 444 (2007) 138–145.
- [10] R. George, K.T. Kashyap, R. Rahul, S. Yamdagni, Strengthening in carbon nanotube aluminium (CNT/Al) composites, *Scr. Mater.* 53 (2005) 1159–1163.
- [11] A.M.K. Esavi, M.A. El Boradi, Carbon nanotube-reinforced aluminium strips, *Compos. Sci. Technol.* 68 (2008) 486–492.
- [12] D.W. Richerson, *Modern Ceramic Engineering*, CRT Press, United States of America, 2006, 644.
- [13] W.A. Curtin, B.W. Sheldon, CNT-reinforced ceramics and metals, *Mater. Today* 11 (2004) 44–49.
- [14] R.W. Siegel, S.K. Chang, B.J. Ash, J. Stone, P.M. Ajayan, R.W. Doremus, L.S. Schadler, Mechanical behavior of polymer and ceramic matrix nanocomposites, *Scr. Mater.* 44 (2001) 2061–2064.
- [15] J. Wang, H. Kou, X. Liu, Y. Pan, J. Guo, Reinforcement of mullite matrix with multi-walled carbon nanotubes, *Ceram. Int.* 33 (2007) 719–722.
- [16] A. Duszová, J. Dusza, K. Tomásek, G. Blugan, J. Kueber, Microstructure and properties of carbon nanotube/zirconia composite, *J. Eur. Ceram. Soc.* 28 (2008) 1023–1027.

- [17] T.Y. Luo, T.X. Liang, C.S. Li, Stabilization of cubic zirconia by carbon nanotubes, *Mater. Sci. Eng. A* 366 (2004) 206–209.
- [18] S.H. Kim, M.R. Zachariah, Gas-phase growth of diameter-controlled carbon nanotubes, *Mater. Lett.* 61 (2007) 2079–2083.
- [19] S. Iijima, T. Ichihashi, Single shell carbon nanotubes of one nanometer diameter, *Nature* 363 (1993) 603–605.
- [20] T. Guo, P. Nikolaev, A. Thess, D.T. Colbert, Catalytic growth of single-walled nanotubes by laser vaporization, *Chem. Phys. Lett.* 243 (1995) 49–54.
- [21] H.L. Ma, D.S. Su, A. Klein-Hoffmann, G.H. Jin, X.Y. Guo, Morphologies and microstructures of free-like carbon produced at different reaction conditions in a CVD process, *Carbon* 44 (2006) 2254–2260.
- [22] L. Kumari, T. Zhang, G.H. Du, W.Z. Li, Q.W. Wang, A. Datye, K.H. Wu, Thermal properties of CNT–alumina nanocomposites, *Compos. Sci. Technol.* 68 (2008) 2178–2183.
- [23] P.J.F. Harris, *Carbon Nanotube Science*, Cambridge University Press, United Kingdom, 2009. 55.
- [24] R. Philippe, A. Morançais, M. Corrias, B. Caussat, Y. Kihn, P. Kalck, D. Plee, P. Gaillard, D. Bernard, P. Serp, Catalytic production of carbon nanotubes by fluidized-bed CVD, *Chem. Vap. Depos.* 13 (2007) 447–457.
- [25] S. Xie, W. Li, Z. Pan, B. Chang, L. Sun, Carbon nanotube arrays, *Mater. Sci. Eng. A* 246 (2000) 11–15.
- [26] B. Chan, S.I. Cha, K.T. Kim, K.H. Lee, S.H. Hong, Fabrication of carbon nanotube reinforced alumina matrix nanocomposite by sol–gel process, *Mater. Sci. Eng. A* 395 (2005) 124–128.
- [27] S.I. Cha, K.T. Kim, K.H. Lee, C.B. Mo, S.H. Hong, Strengthening and toughening of carbon nanotube reinforced alumina nanocomposite fabricated by molecular level mixing process, *Scr. Mater.* 53 (2005) 793–797.
- [28] M. Aromaa, H. Keskinen, J.M. Mäkelä, The effect of process parameters on the Liquid Flame Spray generated titania nanoparticles, *Biomol. Eng.* 24 (2007) 543–548.
- [29] J.M. Mäkelä, H. Keskinen, T. Forsblom, J. Keskinen, Generation of metal and metal oxide nanoparticles by liquid flame spray process, *J. Mater. Sci.* 39 (2004) 2783–4788.
- [30] J.-P. Nikkanen, H. Keskinen, M. Aromaa, M. Järn, T. Kanerva, E. Levänen, J.M. Mäkelä, T. Mäntylä, Iron oxide doped alumina-zirconia nanoparticle synthesis by liquid flame spray from metal organic precursors, *Res. Lett. Nanotechnol.* (2008), <http://dx.doi.org/10.1155/2008/516478>.
- [31] B.D. Cullity, *Elements of X-ray Diffraction*, Addison-Wesley Publishing Company, Inc., 1967. 98.
- [32] R. Mueller, R. Jossen, S.E. Pratsinis, M. Watson, M.K. Akhtar, Zirconia nanoparticles made in spray flames at high production rates, *J. Am. Ceram. Soc.* 87 (2004) 197–202.
- [33] A.H. Heuer, L.W. Hobbs, *Advances in Ceramics: Science and Technology of Zirconia*, The American Ceramic Society, Inc., Columbus, 1981. 1–5.
- [34] J. Chandradass, D.S. Bae, Nano  $\alpha$ - $\text{Al}_2\text{O}_3$ - $\text{t-ZrO}_2$  composite powders by calcining an emulsion precursor at 1100 °C, *J. Alloys Compd.* 469 (2008) 10–12.
- [35] W.J. Kim, J.Y. Park, S.J. Oh, Y.S. Kim, I.H. Kuku, Microstructure of  $\text{Al}_2\text{O}_3$ - $\text{ZrO}_3$  nanocomposites prepared by combustion process, *J. Mater. Sci. Lett.* 16 (1997) 719–721.
- [36] P.C.J. Graat, M.A.J. Somers, Simultaneous determination of composition and thickness of thin iron-oxide films from XPS Fe 2p spectra, *Appl. Surf. Sci.* 100 (1996) 36–40.
- [37] W. Kündig, H. Bömmel, G. Konstabaris, R.H. Lindquist, Some properties of supported small  $\alpha$ - $\text{Fe}_2\text{O}_3$ , *Phys. Rev.* 142 (1966) 327–333.
- [38] P. Karen, K. Gustafsson, J. Lindén, Extent of charge ordering by Mössbauer spectroscopy and high-intensity high-resolution powder diffraction, *J. Solid State Chem.* 180 (2007) 138–147.
- [39] I.K. Herrmann, R.N. Grass, W.J. Stark, High-strength metal nanomagnets for diagnostics and medicine, *Nanomedicine* 4 (2009) 787–798.
- [40] A. Jorio, M.A. Pimenta, A.G. Souza Filho, R. Saito, G. Dresselhaus, M.S. Dresselhaus, Characterizing carbon nanotube samples with resonance Raman scattering, *New J. Phys.* 5 (2003) 139.1–139.17.
- [41] R.A. DiLeo, B.J. Landi, R.P. Raffaele, Purity assessment of multiwalled carbon nanotubes by Raman spectroscopy, *J. Appl. Phys.* 101 (2007) 064307.
- [42] P.T. Araujo, S.K. Doorn, S. Kilina, S. Tretiak, E. Einarsson, S. Maruyama, H. Chacham, M.A. Pimenta, A. Jorio, Third and fourth optical transitions in semiconducting carbon nanotubes, *Phys. Rev. Lett.* 98 (2007) 067401.
- [43] G. Wu, J. Zhou, J. Dong, Radial-breathing-like phonon modes of double-walled carbon nanotubes, *Phys. Rev. B* 72 (2005) 115418.
- [44] D. Bom, R. Andrews, D. Jacques, J. Aanthony, B. Chen, M.S. Meier, J.P. Selegue, Thermogravimetric analysis of the oxidation of multiwalled carbon nanotubes: evidence for the role of defect sites in carbon nanotube chemistry, *Nano Lett.* 2 (2002) 615–619.